












Molecular beam epitaxy of single-crystalline bixbyite $(\text{In}_{1-x}\text{Ga}_x)_2\text{O}_3$ films ($x \leq 0.18$): Structural properties and consequences of compositional inhomogeneity

Alexandra Papadogianni ¹, Charlotte Wouters,² Robert Schewski ², Johannes Feldl ¹, Jonas Lähnemann ¹,
Takahiro Nagata ³, Elias Kluth ⁴, Martin Feneberg ⁴, Rüdiger Goldhahn ⁴, Manfred Ramsteiner ¹,
Martin Albrecht ² and Oliver Bierwagen ^{1,*}

¹Paul-Drude-Institut für Festkörperelektronik, Leibniz-Institut im Forschungsverbund Berlin e.V.,
Hausvogteiplatz 5–7, 10117 Berlin, Germany

²Leibniz-Institut für Kristallzüchtung, Max-Born-Strasse 2, 12489 Berlin, Germany

³National Institute for Materials Science, 1-1 Namiki, Tsukuba, Ibaraki 305-0044, Japan

⁴Institut für Experimentelle Physik, Otto-von-Guericke-Universität Magdeburg, Universitätsplatz 2, 39106 Magdeburg, Germany



(Received 21 June 2021; accepted 20 January 2022; published 14 March 2022)

We report the heteroepitaxial growth of single-crystalline bixbyite $(\text{In}_{1-x}\text{Ga}_x)_2\text{O}_3$ films on (111)-oriented yttria-stabilized zirconia substrates using plasma-assisted molecular beam epitaxy. A pure In_2O_3 buffer layer between the substrate and $(\text{In}_{1-x}\text{Ga}_x)_2\text{O}_3$ alloy is shown to result in smoother film surfaces and significantly improved crystallinity. Transmission electron microscopy confirms the single crystallinity up to $x = 0.18$ and only slight film quality deterioration with increasing Ga content. X-ray diffraction demonstrates partially relaxed layers with lattice parameters fitting well to Vegard's law. However, the Ga cations are not evenly distributed within the films containing nominally $x > 0.11$: inclusions with high Ga density up to $x = 0.50$ are observed within a “matrix” with $x \approx 0.08$. The cubic bixbyite phase is preserved in both the matrix and the inclusions, which is in contrast to previous work reporting secondary, Ga-rich monoclinic or hexagonal phases forming beyond the solubility limit (of $x \approx 0.10$) of Ga in bixbyite In_2O_3 . Moreover, for $x \geq 0.11$, both the Raman phonon lines and the optical absorption onset remain nearly constant. Hard x-ray photoelectron spectroscopy measurements also indicate a widening of the band gap and exhibit similar saturation of the Ga $2p$ core level position for high Ga contents. This saturation behavior of the spectroscopic properties largely reflects the properties of the matrix of the film, while the results of x-ray diffraction are related only to the average (matrix and inclusions) film composition.

DOI: [10.1103/PhysRevMaterials.6.033604](https://doi.org/10.1103/PhysRevMaterials.6.033604)

I. INTRODUCTION

The group-III sesquioxides In_2O_3 and Ga_2O_3 are transparent semiconducting materials widely studied both for their implementation in electronic devices and, from a fundamental semiconductor physics perspective, for their unique properties. Although these two oxide compounds are isovalent and have the same chemical configuration, the equilibrium structures of In_2O_3 and Ga_2O_3 are very different, which can be explained in terms of Coulomb and orbital interactions, influenced by cation size and valence electron energies, respectively [1].

On the one hand, In_2O_3 has a stable cubic bixbyite crystal structure and belongs to space group 206 ($Ia\bar{3}$) with a lattice parameter of $a_{\text{In}_2\text{O}_3} = 10.117 \text{ \AA}$ [2], as well as a less studied metastable rhombohedral structure of space group 167 ($R\bar{3}c$). Bixbyite In_2O_3 possesses an optically forbidden direct band gap of approximately 2.7–2.9 eV, with strong optical absorption occurring from valence bands nearly 1 eV below the valence band maximum [3–5], resulting in the onset of strong optical absorption at around 3.7 eV. This property of In_2O_3 renders it transparent in the visible regime and is remarkably

combined with high electrical conductivity because In_2O_3 exhibits inherent n -type conductivity due to what is commonly referred to as unintentional doping. This unintentional conductivity can be significantly enhanced by intentional donor doping. Sn-doped In_2O_3 —commonly known as indium tin oxide [6–8]—is the most widely commercially used transparent conducting oxide (TCO) as a transparent contact in optoelectronics, such as displays, light-emitting diodes, and solar cells.

On the other hand, Ga_2O_3 , which has been in the spotlight for the past few years, has attracted interest for applications in ultraviolet (UV) photodetectors and power-electronics devices. It has several polymorphs [9,10], the most stable of which is its β phase. β - Ga_2O_3 has a monoclinic crystal structure, which belongs to space group 12 ($C2/m$), and possesses a band gap of approximately 4.8 eV [11]. It is thus transparent both within the visible range and well into the UV range. A bixbyite “ δ ”- Ga_2O_3 phase has been theoretically predicted to have a lattice parameter of approximately $a_{\text{Ga}_2\text{O}_3} = 9.190\text{--}9.401 \text{ \AA}$ [12,13] and a band gap of 5.0 eV, according to the latest report [12]. To our knowledge, this phase has not been experimentally demonstrated yet [14], despite the early reports of Roy *et al.* [9]. Finally, in contrast to In_2O_3 , high-quality, pure Ga_2O_3 films are insulating at room temperature [15].

*bierwagen@pdi-berlin.de

A combination of these two oxides allows for adjustments of the properties of the two original compounds and can, for instance, facilitate band gap engineering [16], as observed in other semiconductor systems. Moreover, concerning potential applications, the incorporation of Ga in the In_2O_3 crystal lattice would potentially provide us with a wide-band-gap TCO, assuming that additional doping with Sn can be achieved. Several studies have been done in this direction, with films prepared by various techniques covering the entire composition range of $(\text{In}_{1-x}\text{Ga}_x)_2\text{O}_3$ [17], although most of the works found in the literature focus on the high- x , Ga-rich end [18–21]. Due to the different crystal structures of the parent materials, structural changes over the composition range are expected, which should limit their miscibility and affect the electronic properties of the resulting alloy. Density-functional theory calculations estimate that the miscibility gap opens at $x = 0.15$ for freestanding $(\text{In}_{1-x}\text{Ga}_x)_2\text{O}_3$ and at $x = 0.45$ for the bixbyite alloy grown epitaxially on In_2O_3 , independent of the growth temperature [22]. The recent work of Wouters *et al.* [23] predicts the cubic phase is stable up to approximately $x = 0.10$, in agreement with the accompanying transmission electron microscopy of pulsed-laser-deposition (PLD) grown $(\text{In}_{1-x}\text{Ga}_x)_2\text{O}_3$ thin films as well as with previous experimental investigations of $(\text{In}_{1-x}\text{Ga}_x)_2\text{O}_3$ polycrystalline bulk ceramic alloys [24,25] that identified the Ga solubility of $x \approx 0.10$ in the cubic phase. At higher Ga content, the excess Ga has been found to precipitate as a secondary β - Ga_2O_3 phase in bulk ceramics [24,26] and a mixture of secondary monoclinic and hexagonal $(\text{In}, \text{Ga})_2\text{O}_3$ phases in PLD-grown films [23]. Further experimental studies on thin films grown by metal-organic chemical vapor deposition [27] and combinatorial PLD [28,29] suggest single-phase bixbyite films even for Ga contents up to $x = 0.50$ and 0.25 to 0.40 , respectively, gauged only by symmetric out-of-plane 2θ - ω x-ray diffraction (XRD) scans. We note, however, that these XRD scans are rather

insensitive to potentially present misaligned secondary phase crystallites or amorphous regions and are thus insufficient to prove phase purity. Hence, there is still a lack of studies with detailed structural information on well-defined high-quality, single-phase $(\text{In}_{1-x}\text{Ga}_x)_2\text{O}_3$ films with low x , allowing for deep exploration of the fundamental physical properties of the bixbyite phase of this alloy.

In this work, we elaborate the synthesis of single-crystalline, phase-pure $(\text{In}_{1-x}\text{Ga}_x)_2\text{O}_3$ thin films up to $x = 0.18$ using plasma-assisted molecular beam epitaxy (PA-MBE). The resulting films served as the basis for our studies on the optical and phonon [30] as well as electron transport properties [31] of single-phase bixbyite $(\text{In}_{1-x}\text{Ga}_x)_2\text{O}_3$. In the present work, the films are evaluated in terms of morphology, crystallinity, lattice parameters, and compositional homogeneity. Ga beyond the classical solubility limit is found to precipitate in inclusions with Ga content up to $x = 50\%$. Contrary to previous theoretical predictions as well as experimental findings in bulk ceramics and PLD-grown material [23,24], these inclusions maintain the bixbyite crystal structure in our case. This compositional inhomogeneity is shown to result in a saturation behavior of spectroscopic properties with increasing Ga content x .

II. EXPERIMENTAL DETAILS

For the purposes of this study, high-quality (111)-oriented single-crystalline $(\text{In}_{1-x}\text{Ga}_x)_2\text{O}_3$ films were synthesized by PA-MBE on insulating $\text{ZrO}_2\text{:Y}$ (YSZ) (111) substrates. The study focuses on the low- x bixbyite phase end of $(\text{In}_{1-x}\text{Ga}_x)_2\text{O}_3$; hence, the substrate choice is based on its suitability for heteroepitaxy of pure In_2O_3 . Along the [100] direction In_2O_3 crystallizes on a 2×2 YSZ unit cell with a cube-on-cube epitaxial relation [32] with a low tensile mismatch of 1.6%–1.7% [33,34] as In_2O_3 has a lattice constant of

TABLE I. Growth parameters for $(\text{In}_{1-x}\text{Ga}_x)_2\text{O}_3$ samples on YSZ (111): T_{nucl} denotes the substrate temperature during the nucleation process of the pure In_2O_3 buffer layer (with the exception of sample Ib, where Ga was also provided), T_{max} is the maximum substrate temperature reached during the smoothing process, and T_{growth} is the final growth temperature. t_{nucl} and t_{growth} are the growth times for the nucleation layer and the bulk of the film, respectively. O flux corresponds to the oxygen flux used for both the nucleation and growth, and the value in brackets for series III corresponds to the increased value during the growth interruption and surface smoothing. $\text{BEP}_{\text{In/Ga}}$ is the beam equivalent pressure of the respective metal cell. d_{film} is the total thickness of the resulting film (including the buffer layer). x_{EDX} is the corresponding Ga cation content, given in cation percentage, as measured on the as-grown samples by energy dispersive x-ray spectroscopy (EDX). $R_q^{10\mu\text{m}}$ is the rms roughness of a $10 \times 10 \mu\text{m}^2$ AFM image, and $\omega_{\text{FWHM}}^{222}$ is the FWHM of the rocking curve of the $(\text{In}, \text{Ga})_2\text{O}_3$ 222 peak.

Series	Sample	T_{nucl} (°C)	T_{max} (°C)	T_{growth} (°C)	t_{nucl} (s)	t_{growth} (s)	O flux (sccm)	BEP_{In} (10^{-7} mbar)	BEP_{Ga} (10^{-8} mbar)	BEP_{Sn} (10^{-8} mbar)	d_{film} (nm)	x_{EDX}	In_2O_3 buffer	$R_q^{10\mu\text{m}}$ (nm)	$\omega_{\text{FWHM}}^{222}$ (deg)
I	a	600	750	750	270	2400	0.5	4.0			294			2.3	0.23
	b							4.2	2.6		294	0.12	no	27	2.70
	c							4.2	2.6		267	0.12	yes	19	0.35
II	a	600	750	600	270	2400	0.5	5.4			326			1.8	0.31
	b							5.4	2.5		312	0.11	yes	6.4	0.50
	c							5.5	4.0		375	0.14	yes	8.6	0.36
	d							5.5	7.5		356	0.18	yes	11	0.55
III	a	500	650	600	300	2400	1.0 [3.0]	5.3			647			1.6	0.23
	b							5.3	1.3		667	0.05	yes	1.7	0.19
	c							5.5	2.5		703	0.08	yes	2.0	0.31
	d							5.5	3.7		638	0.10	yes	2.5	0.32
	e							5.3	2.4	1.9	664	0.08	yes	7.9	0.27

10.117 Å [2]—slightly smaller than twice that of YSZ for a Y concentration of 10 mol % [35] (such as the ones used in this study), which amounts to approximately 10.28 Å. The choice to grow the (111) surface of In_2O_3 was based on the fact that the (111) plane has the lowest surface tension, i.e., surface free energy per unit area, compared to the other low-index surfaces of In_2O_3 [36], which facilitates the growth of smooth, unfaceted films [37].

Table I summarizes the growth parameters used for the growth of the samples investigated in this study. Oxygen fluxes of 0.5 sccm (sample series I and II) and 1.0 sccm (sample series III), according to Ref. [38], correspond to activated oxygen fluxes that can provide growth rates of 2.2 and 4.4 Å/s, respectively, under stoichiometric growth conditions. The In cell (7N purity) temperature was kept at approximately 810 °C (I and II) and 870 °C (III), providing beam equivalent pressures (BEPs) around $\text{BEP}_{\text{In}} = 5 \times 10^{-7}$ mbar, whereas the Ga cell (7N purity) temperature was varied to provide samples with different Ga cation concentrations. One Sn-doped (indium-gallium-tin oxide) film (sample IIIe) was grown using an additional Sn flux with $\text{BEP}_{\text{Sn}} = 1.9 \times 10^{-8}$ mbar, as seen in Table I. The metal fluxes limited the growth rate of the films to approximately 1.3 Å/s (I and II) to 2.2 Å/s (III); hence, the film development was realized within the O-rich regime. The substrate was continuously rotated around its normal axis during the entire growth process in order to get films with a homogeneous thickness distribution.

Three separate sample series were synthesized at different combinations of nucleation and film growth substrate temperatures, measured by a thermocouple between the substrate heater and the substrate, as well as different oxygen fluxes, as indicated in Table I. Sample series I was realized with the intention to probe the effect of an approximately 40 nm thick pure In_2O_3 buffer layer, which also acted as a nucleation layer, between the substrate and $(\text{In}_{1-x}\text{Ga}_x)_2\text{O}_3$ films, as it was suspected to improve the crystalline quality of the alloy films. As explored in Ref. [39], this was indeed the case, and based on this finding, series II and III were both grown using such a buffer layer (approximately 40 and 80 nm thick, respectively). Inspired by the work of Franceschi *et al.* [40], the growth was interrupted after the nucleation of the buffer layer, and the substrate was heated up to T_{max} as indicated in Table I to provide films with an enhanced smoothness. The samples of series III, in particular, were additionally exposed to an increased O flux of 3 sccm during this interruption. Once T_{max} was reached, the sample remained under these conditions for 10 min before the substrate was cooled down to the final growth temperature T_{growth} .

Throughout the entire growth process, the growth rate was probed by means of laser reflectometry (LR). The resulting film thicknesses from the total growth time and LR growth rate match very well those obtained by cross-sectional scanning electron microscope (SEM) imaging performed later, as specified in Table I. Postgrowth energy dispersive x-ray spectroscopy (EDX) measurements were carried out on the films with a low magnification to identify their average Ga composition. Out-of-plane XRD $2\theta - \omega$ scans and rocking curves (ω scans) determined the phase purity and crystalline quality of the layers, and reciprocal space mapping (RSM) of the $(\text{In}_{1-x}\text{Ga}_x)_2\text{O}_3$ 844 reflex in a grazing exit alignment was

employed to gauge the degree of relaxation of the films and extract their relaxed lattice parameters. Moreover, the single crystallinity of the films was confirmed by transmission electron microscopy (TEM) measurements in a cross-sectional view along the $[1\bar{1}0]$ direction of the substrate, and the surface morphology of the films was characterized by atomic force microscopy (AFM). Raman spectroscopy measurements in backscattering geometry from the surfaces of the epitaxial films were used to investigate the dependence of phonon frequencies on the Ga content, and the optical absorption onset of the alloy films was investigated by spectroscopic ellipsometry in the visible and ultraviolet spectral range (from 0.5 to 6.5 eV). Finally, the electronic states of the bulk of the films were investigated by hard x-ray ($h\nu = 5.95$ keV) photoelectron spectroscopy (HAXPES). A detailed description of the *ex situ* characterization methods can be found in Ref. [39].

III. RESULTS AND DISCUSSION

A. Surface morphology

As In_2O_3 does not easily wet the YSZ substrate [41], the substrate temperature used for the growth of, especially, the initial few nanometers of the epilayer has a clear effect on its crystalline quality, which is also confirmed by the comparison of three pure In_2O_3 films (samples Ia, IIa, IIIa) grown at different temperatures, as shown in the AFM images in Fig. 1. Overall increasing roughness and density of morphological features with increasing Ga content can be observed. The average grain size decreases with Ga, in accordance with the findings of Kong *et al.* [27]. This indicates that the incorporation of Ga leads to a lower surface diffusion length. Moreover, lower temperatures result in smoother films with smaller features, an effect which is probably due to the lower nucleation temperatures accompanying the lower growth temperatures, which enhance quasiwetting on YSZ by nucleation of a high density of small islands that quickly coalesce into a closed film [41].

B. Phase purity and lattice parameter

As seen in the wide-range symmetric $2\theta - \omega$ XRD scans in Fig. 2(a), the film with the highest Ga content, $(\text{In}_{0.82}\text{Ga}_{0.18})_2\text{O}_3$, exhibits only one pure, 111-oriented cubic phase. Moreover, no secondary crystalline Ga_2O_3 phases are observed, in contrast to bulk ceramics studies [24,26] as well as a previous investigation on films grown by PA-MBE containing higher amounts of Ga [42]. The observed low full width at half maximum (FWHM) values from the rocking curves in Fig. 2(b), $\omega_{\text{FWHM}}^{222}$, indicate high crystalline quality. However, an overall increase of $\omega_{\text{FWHM}}^{222}$ with increasing Ga content is exhibited, which is consistent with a slight deterioration of film quality. The lower-intensity features on the right of the $(\text{In}_{1-x}\text{Ga}_x)_2\text{O}_3$ peak could point towards compositional inhomogeneity in the film; however, considering the 2θ values at which they arise, they could also be attributed to interference fringes from the high-quality thin In_2O_3 buffer layer at the interface. The observed shift of the layer peak towards larger 2θ values is expected, as it reflects the decrease of the lattice constant from that of In_2O_3 towards the theoretically predicted one of cubic Ga_2O_3 . Since both parent components,

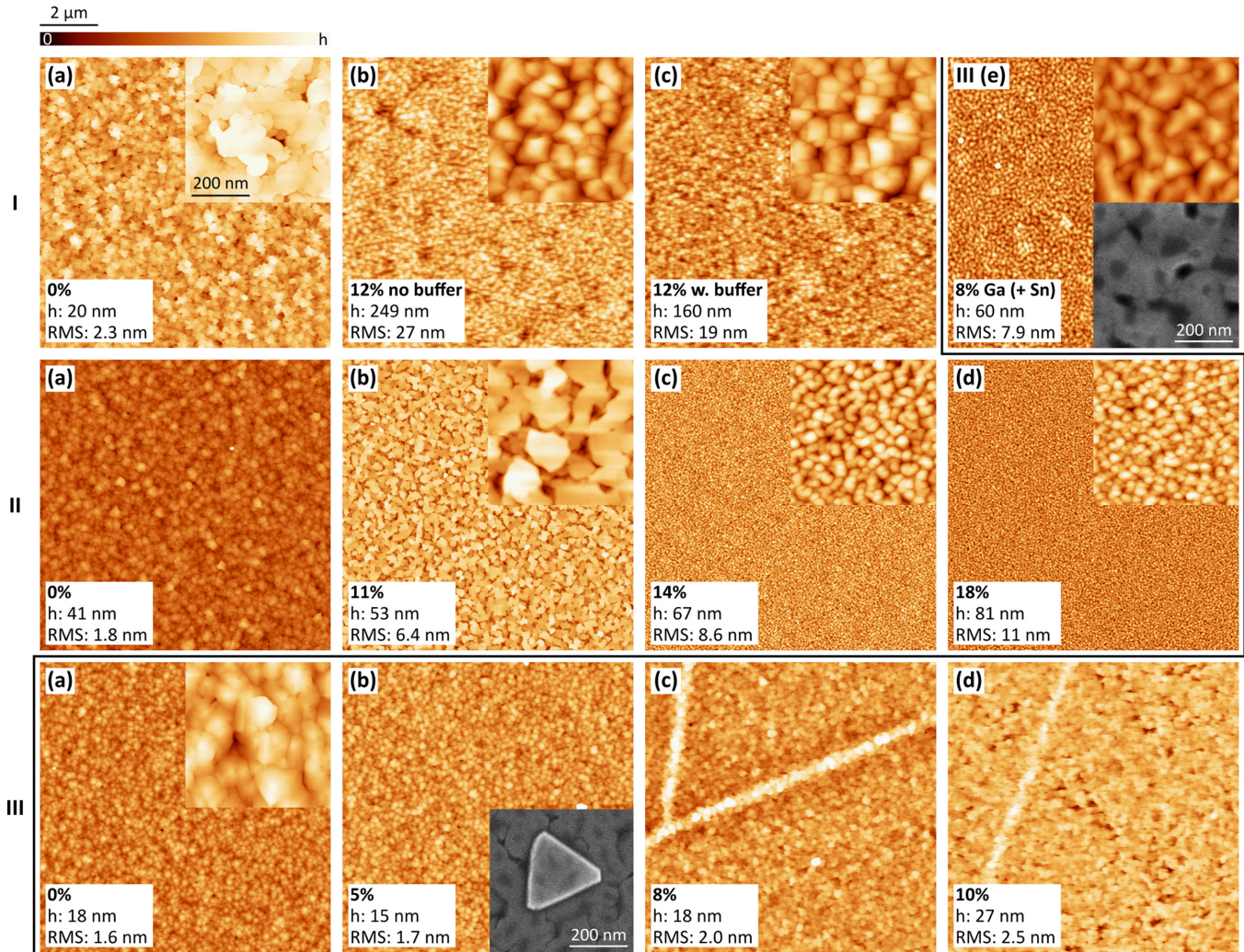


FIG. 1. $10 \times 10 \mu\text{m}^2$ atomic force micrographs of the $(\text{In}_{1-x}\text{Ga}_x)_2\text{O}_3$ films with growth parameters as described in detail in Table I (insets: $1 \times 1 \mu\text{m}^2$). Nucleation and growth temperatures are highest for sample series I and lowest for series III, and Ga content x increases from left to right, explicitly indicated in percentage form. The height scale of the images is indicated by the colored bar at the top and corresponding h in each image. The rms value, also mentioned in Table I, indicates the roughness of the films. The grayscale insets in (b) and (e) for series III are close-up scanning electron microscopy images showing the triangular shape of features on the film surface.

i.e., In_2O_3 and the theoretically predicted bixbyite Ga_2O_3 , have the same crystal structure in their pure forms, Vegard's law can be applied to obtain the relaxed lattice parameter of the alloy:

$$a_{0,(\text{In}_{1-x}\text{Ga}_x)_2\text{O}_3} = (1-x)a_{0,\text{In}_2\text{O}_3} + xa_{0,\text{Ga}_2\text{O}_3}. \quad (1)$$

However, the peak position of measurements like those in Fig. 2 provides information about only the out-of-plane lattice parameter. In order to gain knowledge of the relaxed lattice parameter of the layers, which is affected by both in- and out-of-plane strains, RSMs have been obtained for the films of series II and III. These were performed at an asymmetrical grazing exit alignment in a range of 2θ and ω values that included the 422 reflex of the YSZ substrate and 844 reflex of the $(\text{In}_{1-x}\text{Ga}_x)_2\text{O}_3$ film. An example of such a map can be seen in Fig. 3(a). The (422) and (844) planes can be de-

composed into components parallel and perpendicular to the lattice plane as

$$(422) = \frac{2}{3}(2\bar{1}\bar{1}) + \frac{8}{3}(111), \quad (2a)$$

$$(844) = \frac{4}{3}(2\bar{1}\bar{1}) + \frac{16}{3}(111). \quad (2b)$$

The corresponding reciprocal lattice vectors $Q_{[2\bar{1}\bar{1}]}$ and $Q_{[111]}$ along those two directions are

$$Q_{[2\bar{1}\bar{1}]} = \frac{\cos(\omega) - \cos(2\theta - \omega)}{2}, \quad (3)$$

$$Q_{[111]} = \frac{\sin(\omega) + \sin(2\theta - \omega)}{2}, \quad (4)$$

where ω and 2θ are the incidence and diffraction angles in radians, respectively. All cubic materials should have the same ratio of in- and out-of-plane lattice components; that is, for a fully relaxed layer, in a map plotted in terms of $Q_{[2\bar{1}\bar{1}]}$ and $Q_{[111]}$ such as the one in Fig. 3(a), we would expect the $(\text{In}_{1-x}\text{Ga}_x)_2\text{O}_3$ 844 peak to lie on the same line connecting the

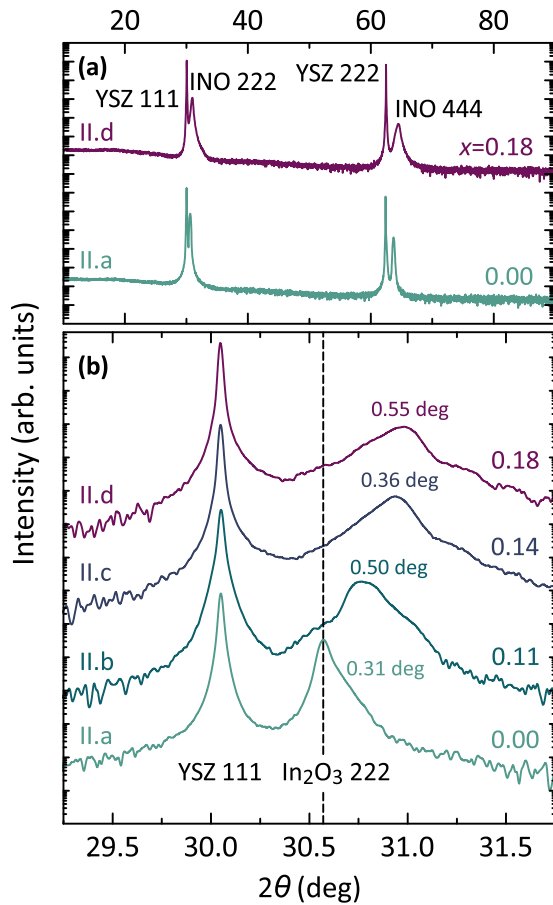


FIG. 2. Symmetric $2\theta - \omega$ XRD scans of sample series II. (a) Broad scan including two reflex orders, showing no additional crystalline phases. (b) Narrow scan around the 111 reflex of the substrate (left peak) and the 222 reflex of the layer (right). The layer peak shifts towards larger angles with additional Ga. The numbers above the layer peaks are the FWHM of the rocking curves of the respective layer peak.

$(Q_{[2\bar{1}\bar{1}]}, Q_{[111]}) = (0, 0)$ point and the 422 peak of the cubic YSZ substrate. For a pseudomorphically strained film, the grown film would assume the in-plane lattice parameter of the substrate; hence, the in-plane components $Q_{[2\bar{1}\bar{1}]}$ of both should be equal. Based on this, it can be concluded that sample IIb is almost fully relaxed. The same applies to all other films grown for this study, the maps of which are not plotted here.

The in- and out-of-plane lattice spacings between adjacent $(\text{In}_{1-x}\text{Ga}_x)_2\text{O}_3$ lattice planes can be calculated from $Q_{[2\bar{1}\bar{1}]}$ and $Q_{[111]}$ as

$$d_{\left(\frac{8}{3} \frac{4}{3} \frac{4}{3}\right)} = \frac{\lambda}{2|Q_{[2\bar{1}\bar{1}]}|}, \quad (5a)$$

$$d_{\left(\frac{16}{3} \frac{16}{3} \frac{16}{3}\right)} = \frac{\lambda}{2Q_{[111]}}, \quad (5b)$$

where λ is the wavelength of the x rays. The corresponding in- and out-of-plane $(\text{In}_{1-x}\text{Ga}_x)_2\text{O}_3$ lattice constants are

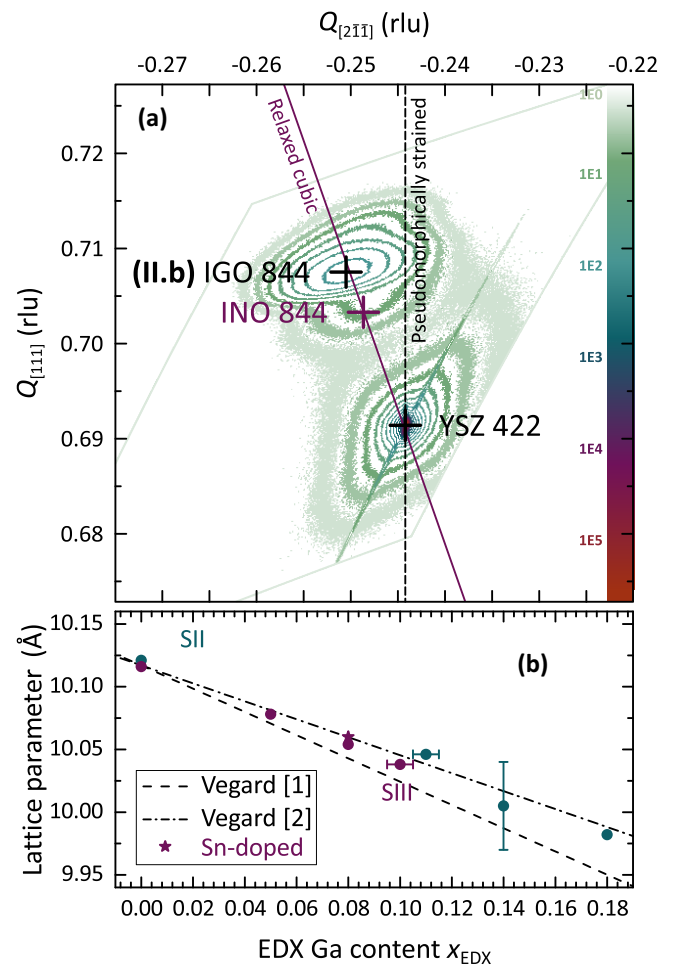


FIG. 3. (a) Example of an RSM at an asymmetrical grazing exit alignment, showing the 422 reflex of the substrate and 844 reflex of the layer (performed on sample IIb). The peak positions of the YSZ substrate and the $(\text{In}_{0.89}\text{Ga}_{0.11})_2\text{O}_3$ film (IIb) are marked by crosses and labeled accordingly, along with the theoretical position of pure In_2O_3 (purple). $Q_{[2\bar{1}\bar{1}]}$ and $Q_{[111]}$, expressed in reciprocal lattice units (rlu), correspond to the in- and out-of-plane directions, respectively. The maps are drawn by equi-intensity lines using a color-coded, logarithmic scale as specified. The vertical dashed and oblique solid lines are guides for pseudomorphically strained and fully relaxed layers, respectively. (b) Ga cation content measured by EDX x_{EDX} and corresponding relaxed lattice parameters a_0 extracted from the RSM measurements. The dashed lines correspond to Vegard's law calculated for the lattice constants of cubic bixbyite Ga_2O_3 in (1) Peelaers *et al.* [12] and (2) Yoshioka *et al.* [13]. The horizontal error bar for samples IIb and SIII is representative of the 1% uncertainty in x_{EDX} and applies to all samples.

calculated using the in- and out-of-plane components of the (844) plane given by Eq. (2b) and

$$a_{[2\bar{1}\bar{1}]} = \frac{4\sqrt{6}}{3} d_{\left(\frac{8}{3} \frac{4}{3} \frac{4}{3}\right)}, \quad (6a)$$

$$a_{[111]} = \frac{16\sqrt{3}}{3} d_{\left(\frac{16}{3} \frac{16}{3} \frac{16}{3}\right)}, \quad (6b)$$

respectively. Based on the values for $a_{[2\bar{1}\bar{1}]}$ and $a_{[111]}$ extracted from the maps and the definition of the Poisson ratio [43]

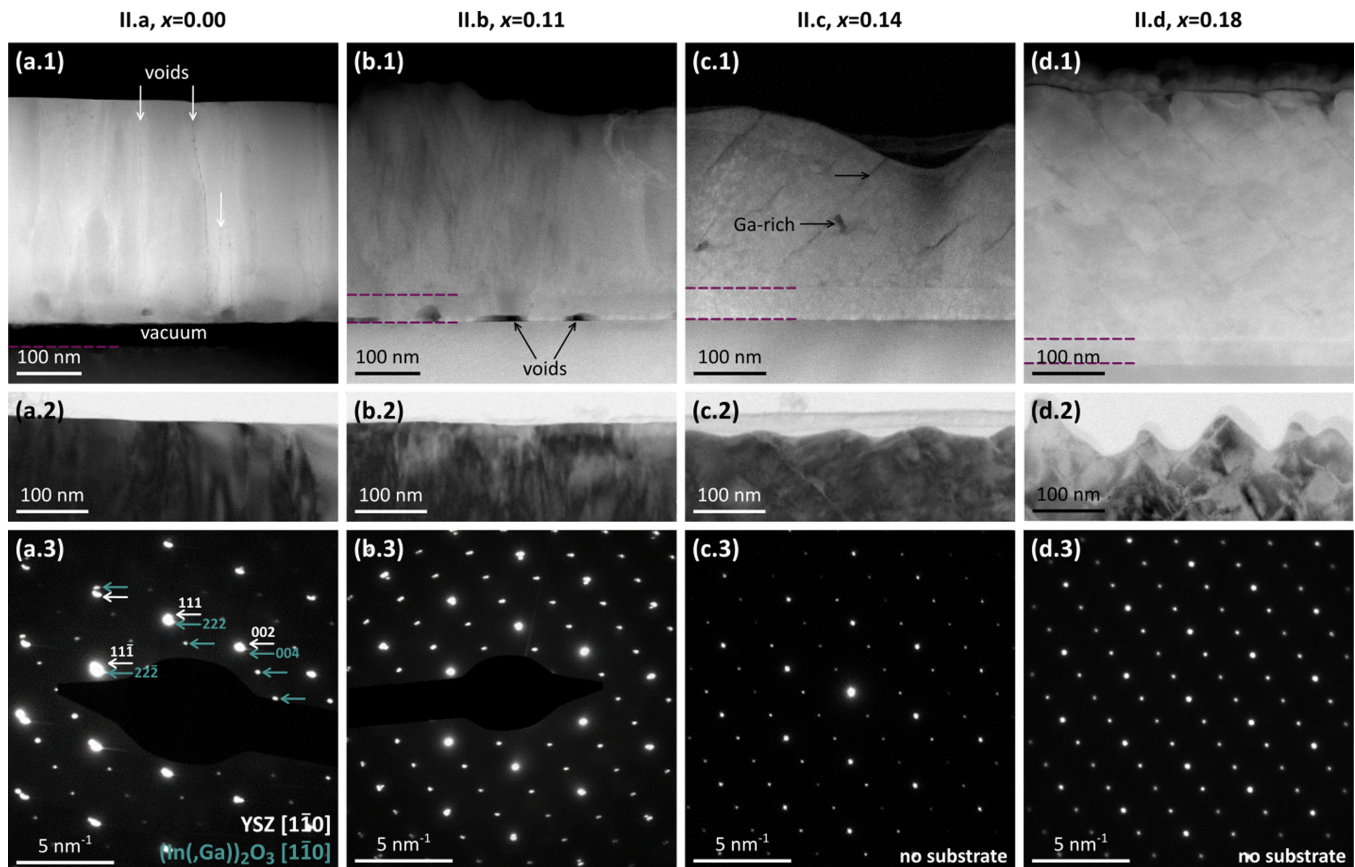


FIG. 4. Top: HAADF-STEM cross-section images of $(\text{In}_{1-x}\text{Ga}_x)_2\text{O}_3$ films with x ranging between 0.00 and 0.18, as indicated. The dashed lines indicate the interfaces between substrate, buffer layer, and film. Middle: Bright field TEM images of the real growth surfaces. Bottom: Electron diffraction patterns of each sample taken in the $[1\bar{1}0]$ orientation, with spots belonging to the YSZ substrate and the layer indexed in white and teal, respectively.

[Eq. (7), where $\varepsilon_{[2\bar{1}\bar{1}], [111]}$ are the in- and out-of-plane strains, respectively], one can calculate the total relaxed lattice parameter a_0 while taking into account that in the case of a cubic crystal the in- and out-of-plane relaxed lattice parameters should be equal:

$$\frac{\varepsilon_{[2\bar{1}\bar{1}]}}{\varepsilon_{[111]}} = \frac{a_{[2\bar{1}\bar{1}]} - a_0}{a_{[111]} - a_0} = -\frac{2\nu}{1-\nu}. \quad (7)$$

Here we used $\nu = 0.31$ obtained experimentally by Zhang *et al.* [44] for 111-oriented In_2O_3 grown on YSZ. Figure 3(b) shows the relaxed lattice parameters a_0 of the alloy films extracted from the RSM measurements as a function of Ga content, as measured by EDX. The obtained a_0 agree reasonably well with the experimental results documented in the earlier work of Regoutz *et al.* [25] on $(\text{In}, \text{Ga})_2\text{O}_3$ ceramics. The plot reveals a roughly linear dependence of the lattice constant on the alloy composition; hence, our films largely follow Vegard's law within the margins of error. The uncertainty in x is approximately 1% for all samples, and uncertainty in a_0 of sample IIc as depicted in Fig. 3(b) is due to significant discrepancies among the various obtained RSMs. The limits posed by the two dashed lines were calculated assuming Vegard's law for the lattice constants of the cubic bixbyite Ga_2O_3 reported in Peelaers *et al.* [12] (9.190 Å, extracted from Fig. 3 therein) and Yoshioka *et al.* [13] (9.40 Å). The agreement with Vegard's law implies the incorporation of Ga cations on In

sites and does not indicate a solubility limit within the x range studied here, which is up to $x = 0.18$. A linear fit of the lattice constant data in Fig. 3(b) lets us estimate an experimental value for the hypothetical cubic bixbyite phase of Ga_2O_3 at 9.365 (± 0.018) Å. Unfortunately, the low intensity and large width of the layer reflexes in the RSMs did not allow the extraction of separate and precise in- and out-of-plane lattice parameters—and therefore strains—that can be systematically explained for the samples with $x \geq 0.10$. This is because the relaxed lattice parameter a_0 is relatively less affected by the reflex position compared to the strain. However, comparing their In_2O_3 reference samples (IIa, IIIa), series II seems to be less strained than series III, which was grown at lower nucleation and final substrate temperatures, with sample IIa showing an in-plane strain of $\varepsilon_{[111]}^{\text{IIa}} \simeq 0.07\%$ and sample IIIa showing $\varepsilon_{[111]}^{\text{IIIa}} \simeq 0.15\%$. We do not expect the alloy films to be significantly more strained and presume an upper strain limit of approximately 0.2%.

The films of sample series II were investigated by TEM to examine their single crystallinity and overall film quality. In the top row of Fig. 4, high-angle annular dark field scanning transmission electron microscopy (HAADF-STEM) images, in which the contrast is proportional to the mean atomic number, of the four epitaxial layers are compared. The surfaces there are affected by the ion milling process, in which the sample is thinned down to electron transparency. The real growth

surfaces are shown right underneath [Figs. 4(a2)–4(d2)] as bright field TEM images. Some voids, likely related to incomplete quasiwetting of the YSZ, can be observed traveling in the form of thin vertical lines through the layer for the pure In_2O_3 as indicated by white arrows and as more extended regions in the film with $x = 0.11$. The films with $x = 0.14$ and $x = 0.18$ do not show such strong voids at the interface and surface and appear rougher, with peak to valley distances of a few tens of nanometers. This suggests that the addition of Ga induces a different growth mode along facets due to a destabilization of the (111) plane. The combined electron diffraction patterns of the substrate and film in Figs. 4(a3)–4(d3) show the presence of a single cubic bixbyite crystalline phase in all samples. All points can be linked to either those of the cubic structure of YSZ or those of the cubic bixbyite structure of the film. Since these lattices have similar cubic symmetries with almost identical lattice parameters—considering a doubling of the periodicity for the bixbyite phase—some spots of the distinct phases overlap and have been indexed twice.

C. Compositional inhomogeneity beyond the Ga solubility limit

Another distinct feature in samples IIc and II d with the nominally highest Ga contents are the dark stripes traveling diagonally upward at a fixed angle through the layer. These features can be identified as regions of increased Ga incorporation according to the EDX analysis of sample IIc, as shown in Fig. 5. EDX point scans on sample IIb with $x = 0.11$ performed in darker and brighter intensity regions of the film show Ga content fluctuations of only 1% (not shown here). This indicates a homogeneous incorporation of the Ga cations in the cubic bixbyite lattice. However, sample IIc with $x = 0.14$ exhibits areas with increased Ga contents varying from $x = 0.20$ up to 0.50 compared to the surrounding “matrix,” which features an average Ga incorporation of approximately $x = 0.08$. This has been identified by EDX line scans crossing the dark features, as shown in Fig. 5(b). One such dark stripe is imaged by HAADF-STEM at high magnification in Fig. 5(a) in the $[1\bar{1}0]$ zone axis orientation of the lattice. The bixbyite structure is preserved throughout the dark stripe without the formation of an additional phase or any lattice defects, which confirms the electron diffraction data indicating that the layer is single phase. The EDX line scans also show a dip in O content coinciding with the Ga increase (see Fig. 2 in the Supplemental Material [39]), indicating void formation as well. The rough surface, the void formation, and the defined orientation of the Ga-rich stripes suggest a faceted three-dimensional island growth, with phase separation resulting from the preferential incorporation of Ga at edges of voids and on well-defined facets. The edge of preferential incorporation seems to correspond to the $(11\bar{1})$ plane (equivalent to 111), as indicated in Fig. 5(a), and the edge travels both laterally and vertically (in the direction of the green arrow) through the layer. Similar Ga-rich features are observed in the MBE growth of AlGaN, where enhanced Ga incorporation is observed on step edges due to a higher Ga desorption rate on the terraces [45]. The $x = 0.18$ sample (not shown here) exhibits similar darker stripes and defects due to relaxation processes through misfit dislocations, as well as

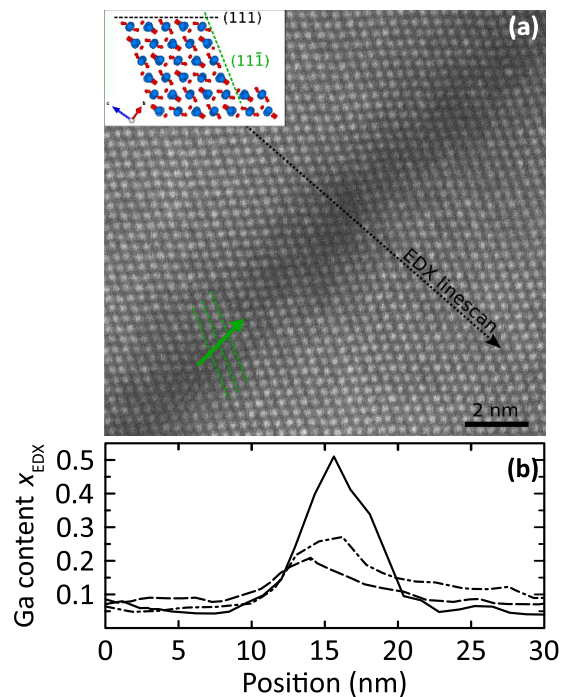


FIG. 5. (a) HAADF-STEM high-magnification image capturing one of the dark stripes traveling through the $(\text{In}_{0.86}\text{Ga}_{0.14})_2\text{O}_3$ (sample IIc). Bright spots correspond to projected atomic (In, Ga) columns (oxygen is too light to produce visible contrast), and the observed pattern fits the bixbyite model structure. The atomic pattern is resolved and fits the model structure of the cubic bixbyite phase in the $[1\bar{1}0]$ orientation. (b) EDX line scans across three different dark stripes showing increased Ga incorporation in these areas.

grains and initial signs of phase separation and amorphicity, but maintains a single cubic phase throughout.

Hence, despite the preservation of the bixbyite phase and the good agreement with Vegard’s law, Ga is inhomogeneously distributed in the samples that exceed the classical Ga solubility limit ($x > 0.11$ in our case). Contrary to previous theoretical and experimental studies [23,24], the excess Ga does not form a separate monoclinic or hexagonal phase in our material, which we relate to the nonequilibrium MBE growth kinetics and nanoscale dimensions of the Ga-rich inclusions. Since the alloy films were grown on pure In_2O_3 buffer layers, the prediction of Maccioni *et al.* [22] of enhanced miscibility of the $(\text{In}_{1-x}\text{Ga}_x)_2\text{O}_3$ alloy up to 45% for epitaxial growth on In_2O_3 could provide an additional explanation for this effect.

D. Saturation of Raman phonon mode shift, optical absorption edge, and Ga 2p core level position

In Ref. [30] a monotonous blueshift with increasing Ga contents up to $x = 0.10$ was observed for several optical phonon modes in MBE-grown $(\text{In}_{1-x}\text{Ga}_x)_2\text{O}_3$ films (sample series III), demonstrating that Raman spectroscopy can be a suitable tool to determine the Ga incorporation in this alloy in the case of homogeneous Ga distribution. Figure 6 displays the frequency of such phonon modes for the samples in series II, which includes films with nominally $x > 0.10$, along with the data reported in Ref. [30]. The Raman spectra of all alloy

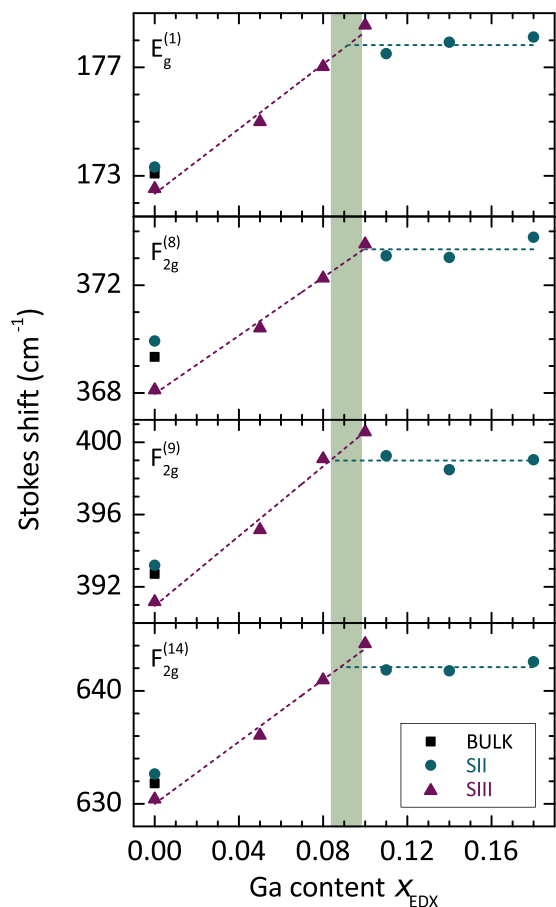


FIG. 6. Frequencies of several optical phonon modes for the epitaxial films of sample series II as a function of the Ga content determined by EDX along with the data for sample series III reported in Ref. [30]. The frequencies of a In_2O_3 bulk sample are shown for reference. Based on the observed linear dependences found for $x < 0.10$, Raman phonon modes imply that even though the samples of series II have nominally $x > 0.10$ based on EDX measurements, the effective Ga incorporation is approximately $x = 0.08$ – 0.09 on average, as indicated by the shaded area.

films exhibit the typical fingerprint of In_2O_3 phonon modes with no indication of additional phases (as in the high-quality bulk crystal in Ref. [46]). The minor discrepancies among the phonon frequencies of the binary In_2O_3 films of different sample series can be potentially attributed to different degrees of lattice strain. Strikingly, the frequencies of all phonon modes remain constant for nominal Ga contents above $x > 0.10$, with the saturation values of the individual phonon frequencies agreeing reasonably well with those obtained for $x = 0.10$ [30]. The absence of a further blueshift with increasing nominal Ga content is most likely related to the findings of the TEM investigations reporting a Ga incorporation of approximately $x = 0.08$ in the main matrix of the film and inclusions with significantly higher Ga content for those films. Apparently, the Raman spectra are dominated by scattering in the matrix of the films and not by the total Ga content of the films. The total volume of the regions with extraordinarily large Ga contents observed by TEM is most likely too small to be detected in the Raman spectra.

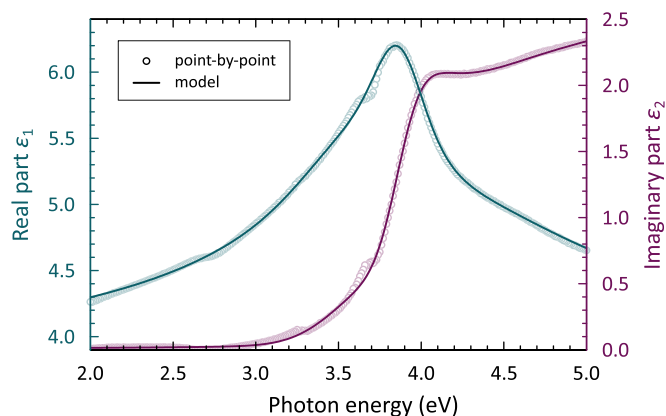


FIG. 7. Real, ϵ_1 , and imaginary, ϵ_2 , parts of the dielectric functions for the $(\text{In}_{0.89}\text{Ga}_{0.11})_2\text{O}_3$ film (sample IIb) determined by spectroscopic ellipsometry. Both the point-by-point fitted result (open circles) and the dielectric function as described by a model function (lines) are shown.

Spectroscopic ellipsometry was demonstrated in Ref. [30] to be a further spectroscopic tool to study the incorporation of Ga in $(\text{In}_{1-x}\text{Ga}_x)_2\text{O}_3$ alloy films. The onset of optical absorption has been shown to exhibit a pronounced blueshift with increasing Ga content for the samples in series III. Regarding sample series II, the dielectric function of the sample with $x = 0.11$ is shown in Fig. 7. A comparison between the dielectric functions of the samples in series II and pure In_2O_3 can be found in the recent work of Feldl *et al.* [30]. The observed blueshift of the absorption onset by 95 meV induced by alloying is somewhat lower than expected based on the results reported in Ref. [30], presumably due to the different growth conditions. Note that many-body corrections such as the Burstein-Moss effect and band gap renormalization can be neglected for the investigated sample [47], which was annealed in oxygen (rapid thermal annealing at a final temperature of 800 °C at atmospheric pressure for 60 s). Due to rough surface morphologies (see Fig. 1), samples with $x > 0.11$ could not be analyzed by spectroscopic ellipsometry. Instead, we developed a method to determine the blueshift of the absorption onset in such alloy films using Raman spectroscopy. Our approach is based on the fact that the relative contribution of Raman scattering in the YSZ substrate is directly correlated with the optical absorption in the $(\text{In}_{1-x}\text{Ga}_x)_2\text{O}_3$ alloy films. Utilizing optical excitation at 3.81 eV (close to the onset of absorption), the intensity of the YSZ substrate signal in Raman spectra can be used to determine the alloying-induced blueshift of the optical absorption onset in those rough samples. A detailed description of our approach and a verification of its validity are presented in the Supplemental Material. The obtained relative optical absorption onsets for $x = 0.14$ and 0.18 are shown in Fig. 8 along with the value determined by spectroscopic ellipsometry for $x = 0.11$ (see Fig. 7). In accordance with the result obtained for the frequencies of optical phonons, no clear dependence of the absorption onset on the nominal Ga content is found for $x > 0.11$ within the limits of accuracy (uncertainty of about 20 meV). Consequently, the saturation of the blueshifts found for both the phonon frequencies and the optical absorption onset confirms the phase

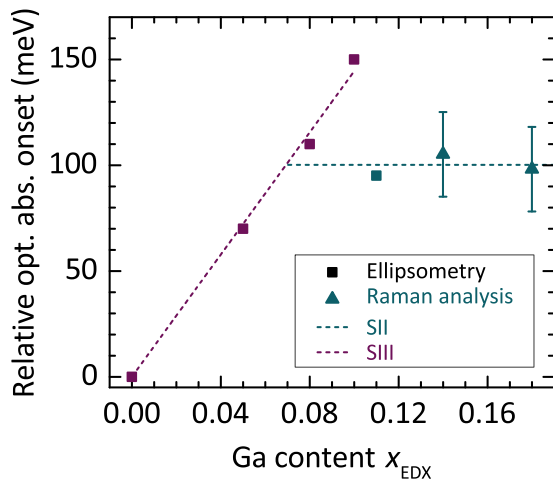


FIG. 8. Shift of the optical absorption onset of alloy films with $x = 0.14$ (sample IIc) and $x = 0.18$ (sample IId) with respect to that of In_2O_3 determined by the analysis of the YSZ substrate signal in Raman spectra (triangles). The corresponding blueshifts of the alloy film with $x = 0.11$ and for sample series III (reported in Ref. [30]) are based on the analysis of the dielectric functions, such as that shown in Fig. 7 for sample IIb. The dashed lines are linear fits of the data of sample series II and III (teal and purple, respectively) and are intended as guides to the eye.

separation observed by TEM for alloy films with nominal Ga contents above about 10%.

Finally, in order to investigate chemical bonding and electronic states of the alloy, the films in series II were investigated using HAXPES. The valence band structures of three of them (IIa, IIb, and IId) can be seen in Fig. 9. For In_2O_3

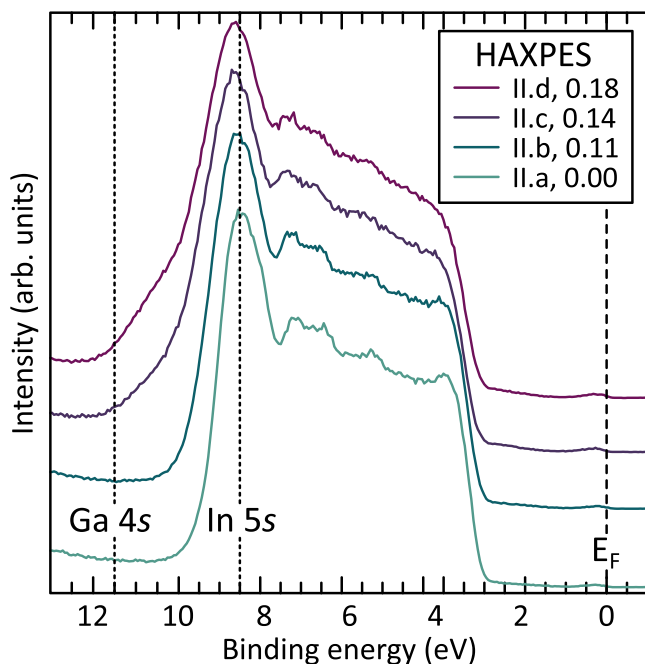


FIG. 9. HAXPES valence band spectra of $(\text{In}_{1-x}\text{Ga}_x)_2\text{O}_3$ with nominal Ga contents of $x = 0.00, 0.11, 0.14,$ and 0.18 (sample series II).

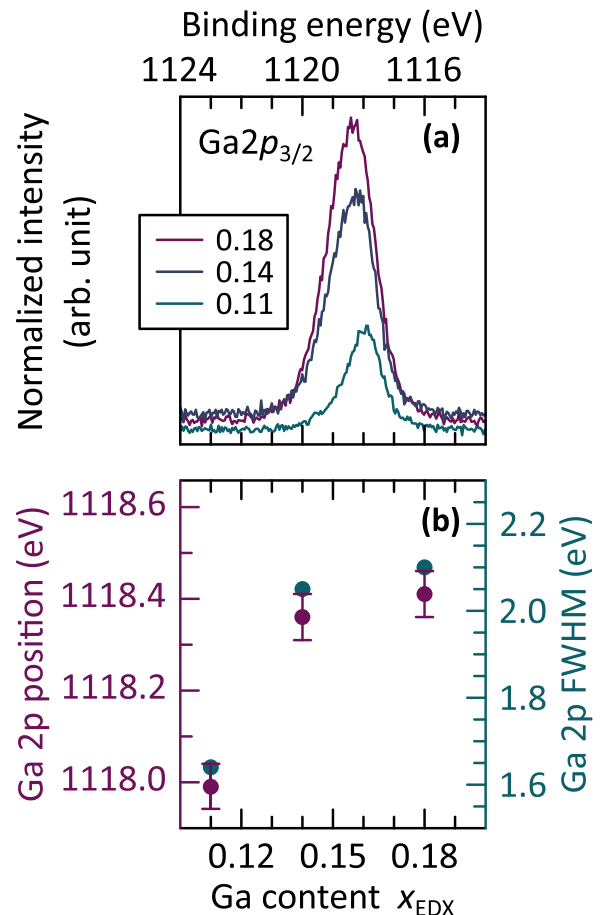


FIG. 10. (a) HAXPES Ga $2p$ core level binding energies and peak shapes and (b) comparison of peak positions of all alloy layers of series II and the corresponding FWHM as a function of Ga content.

and Ga_2O_3 , features around 8.5 and 11.5 eV are expected, corresponding to the In $5s$ and Ga $4s$ orbitals, respectively. As seen in Fig. 9, the addition of Ga shifts the spectrum to higher binding energies. For the IId film with $x = 0.18$, in particular, an additional, distinct feature can be observed at the high-binding-energy end. This can be attributed to the inclusions with very high Ga contents having a distinctly different valence band structure. Charge distributions of the Ga bonding state were confirmed in the Ga $2p$ spectra for all Ga-containing samples in series II, as shown in Fig. 10. Both the peak position and FWHM values of the Ga $2p$ core level change significantly for $x > 0.11$. The saturation of the core level position likely reflects the matrix of the film, similar to the saturation observed in the Raman line frequency shift and optical band gap width.

Hence, the investigations and analysis of the $(\text{In}_{1-x}\text{Ga}_x)_2\text{O}_3$ alloy films using spectroscopic techniques, along with the combination of TEM and EDX data, revealed that XRD results inferring a homogeneous incorporation of the Ga cations up to $x = 0.18$ can be misleading.

IV. CONCLUSION

The heteroepitaxial growth of $(\text{In}_{1-x}\text{Ga}_x)_2\text{O}_3$ on YSZ is enhanced by the employment of a thin pure In_2O_3 buffer layer between the alloy film and the substrate, which provides a better-matched substrate in terms of wetting, chemistry, and lattice parameters. This was demonstrated in terms of small FWHMs of x-ray diffraction rocking curves, which indicate higher film crystallinity, as well as smoother film surfaces. Both x-ray diffraction and transmission electron microscopy investigations confirmed the cubic phase purity and single crystallinity of the films up to nominal Ga contents of $x = 0.18$. The lattice parameters of the films measured by x-ray diffraction reciprocal space mapping obey Vegard's law, assuming the Ga contents measured by energy dispersive x-ray spectroscopy. These findings seem to imply a homogeneous incorporation of Ga in the alloy films.

However, closer inspection of transmission electron micrographs of the samples with the highest Ga compositions and local energy dispersive x-ray spectroscopy measurements revealed Ga-rich inclusions in the films with Ga contents as high as $x = 0.50$, while the remaining film, the matrix, exhibits Ga incorporation at the classical solubility limit (of approximately $x = 0.08$ in our case). Likely related to the nonequilibrium MBE growth kinetics and their nanoscale dimensions, the Ga-rich inclusions maintain the cubic bixbyite structure instead of forming the monoclinic or hexagonal phases reported in previous theoretical and experimental studies. The use of pure In_2O_3 buffer layers probably also benefits the miscibility of the alloy [22].

The analysis of the $(\text{In}_{1-x}\text{Ga}_x)_2\text{O}_3$ alloy films by Raman spectroscopy, spectroscopic ellipsometry, and hard x-ray photoelectron spectroscopy corroborates this compositional inhomogeneity found by TEM. They show systematic shifts up to an average composition of approximately $x = 0.10$ and saturation for further increasing x , in which case their results largely reflect the properties of the larger volume fraction, the matrix, rather than that of the inclusions with high x . In contrast to this behavior, x-ray diffraction and reciprocal space maps rather reflect the average material, i.e., both the matrix and inclusions with high x , since elastic relaxation between areas with different Ga contents takes place.

ACKNOWLEDGMENTS

We would like to thank D. Van Dinh and T. Teubner for critically reading the manuscript, as well as U. Jahn for help with the EDX investigations of the Ga content of the films, A.-K. Bluhm for the cross-sectional SEM images for film thickness characterization, and H.-P. Schönherr and C. Stemmler for technical assistance with the MBE system. This study was performed in the framework of GraFOx, a Leibniz-ScienceCampus partially funded by the Leibniz Association. We are also grateful to HiSOR, Hiroshima University, and JAEA/SPring-8 for the development of HAXPES at BL15XU of SPring-8. The HAXPES measurements were performed under the approval of the NIMS Synchrotron X-ray Station (Proposal No. 2019B4602).

-
- [1] J. Ma and S.-H. Wei, *Comput. Mater. Sci.* **104**, 35 (2015).
 - [2] M. Marezio, *Acta Crystallogr.* **20**, 723 (1966).
 - [3] A. Walsh, J. L. F. Da Silva, S.-H. Wei, C. Körber, A. Klein, L. F. J. Piper, A. DeMasi, K. E. Smith, G. Panaccione, P. Torelli, D. J. Payne, A. Bourlange, and R. G. Egdell, *Phys. Rev. Lett.* **100**, 167402 (2008).
 - [4] P. D. C. King, T. D. Veal, F. Fuchs, C. Y. Wang, D. J. Payne, A. Bourlange, H. Zhang, G. R. Bell, V. Cimalla, O. Ambacher, R. G. Egdell, F. Bechstedt, and C. F. McConville, *Phys. Rev. B* **79**, 205211 (2009).
 - [5] K. Irmscher, M. Naumann, M. Pietsch, Z. Galazka, R. Uecker, T. Schulz, R. Schewski, M. Albrecht, and R. Fornari, *Phys. Status Solidi A* **211**, 54 (2014).
 - [6] G. S. Chae, *Jpn. J. Appl. Phys.* **40**, 1282 (2001).
 - [7] A. N. Tiwari, G. Khrypunov, F. Kurdzesau, D. L. Bätzner, A. Romeo, and H. Zogg, *Prog. Photovoltaics* **12**, 33 (2004).
 - [8] M. Y. Tsai, O. Bierwagen, and J. S. Speck, *Thin Solid Films* **605**, 186 (2016).
 - [9] R. Roy, V. G. Hill, and E. F. Osborn, *J. Am. Chem. Soc.* **74**, 719 (1952).
 - [10] Z. Galazka, *Semicond. Sci. Technol.* **33**, 113001 (2018).
 - [11] T. Matsumoto, M. Aoki, A. Kinoshita, and T. Aono, *Jpn. J. Appl. Phys.* **13**, 1578 (1974).
 - [12] H. Peelaers, D. Steiauf, J. B. Varley, A. Janotti, and C. G. Van de Walle, *Phys. Rev. B* **92**, 085206 (2015).
 - [13] S. Yoshioka, H. Hayashi, A. Kuwabara, F. Oba, K. Matsunaga, and I. Tanaka, *J. Phys.: Condens. Matter* **19**, 346211 (2007).
 - [14] H. Y. Playford, A. C. Hannon, E. R. Barney, and R. I. Walton, *Chemistry - Eur. J.* **19**, 2803 (2013).
 - [15] M. H. Wong, K. Sasaki, A. Kuramata, S. Yamakoshi, and M. Higashiwaki, *Jpn. J. Appl. Phys.* **55**, 1202B9 (2016).
 - [16] R. Hill, *J. Phys. C* **7**, 521 (1974).
 - [17] Y. Kokubun, T. Abe, and S. Nakagomi, *Physica Status Solidi A* **207**, 1741 (2010).
 - [18] V. I. Vasylytsiv, Y. I. Rym, and Y. M. Zakharko, *Phys. Status Solidi B* **195**, 653 (1996).
 - [19] T. Oshima and S. Fujita, *Physica Status Solidi C* **5**, 3113 (2008).
 - [20] M. Baldini, M. Albrecht, D. Gogova, R. Schewski, and G. Wagner, *Semicond. Sci. Technol.* **30**, 024013 (2015).
 - [21] C. Kranert, J. Lenzner, M. Jenderka, M. Lorenz, H. von Wenckstern, R. Schmidt-Grund, and M. Grundmann, *J. Appl. Phys.* **116**, 013505 (2014).
 - [22] M. B. Maccioni, F. Ricci, and V. Fiorentini, *J. Phys.: Condens. Matter* **28**, 224001 (2016).
 - [23] C. Wouters, C. Sutton, L. M. Ghiringhelli, T. Markurt, R. Schewski, A. Hassa, H. von Wenckstern, M. Grundmann, M. Scheffler, and M. Albrecht, *Phys. Rev. Mater.* **4**, 125001 (2020).
 - [24] D. D. Edwards, P. E. Folkins, and T. O. Mason, *J. Am. Ceram. Soc.* **80**, 253 (1997).
 - [25] A. Regoutz, R. Egdell, D. Morgan, R. Palgrave, H. Téllez, S. Skinner, D. Payne, G. Watson, and D. Scanlon, *Appl. Surf. Sci.* **349**, 970 (2015).
 - [26] Y. Liu, W. Xu, D.-B. Liu, M. Yu, Y.-H. Lin, and C.-W. Nan, *Phys. Chem. Chem. Phys.* **17**, 11229 (2015).

- [27] L. Kong, J. Ma, F. Yang, C. Luan, and Z. Zhu, *J. Alloys Compd.* **499**, 75 (2010).
- [28] T. Nagata, T. Hoga, A. Yamashita, T. Asahi, S. Yagyu, and T. Chikyow, *ACS Comb. Sci.* **22**, 433 (2020).
- [29] J. E. N. Swallow, R. G. Palgrave, P. A. E. Murgatroyd, A. Regoutz, M. Lorenz, A. Hassa, M. Grundmann, H. von Wenckstern, J. B. Varley, and T. D. Veal, *ACS Appl. Mater. Interfaces* **13**, 2807 (2021).
- [30] J. Feldl, M. Feneberg, A. Papadogianni, J. Lähnemann, T. Nagata, O. Bierwagen, R. Goldhahn, and M. Ramsteiner, *Appl. Phys. Lett.* **119**, 042101 (2021).
- [31] A. Papadogianni, T. Nagata, and O. Bierwagen, *Jpn. J. Appl. Phys.* (2022), doi: 10.35848/1347-4065/ac4ec7.
- [32] E. J. Tarsa, J. H. English, and J. S. Speck, *Appl. Phys. Lett.* **62**, 2332 (1993).
- [33] R. A. Cowley, A. Bourlange, J. L. Hutchison, K. H. L. Zhang, A. M. Korsunsky, and R. G. Egdell, *Phys. Rev. B* **82**, 165312 (2010).
- [34] O. Bierwagen, M. E. White, M.-Y. Tsai, and J. S. Speck, *Appl. Phys. Lett.* **95**, 262105 (2009).
- [35] H. Hayashi, T. Saitou, N. Maruyama, H. Inaba, K. Kawamura, and M. Mori, *Solid State Ionics* **176**, 613 (2005).
- [36] P. Ágoston and K. Albe, *Phys. Rev. B* **84**, 045311 (2011).
- [37] O. Bierwagen, J. Rombach, and J. S. Speck, *J. Phys.: Condens. Matter* **28**, 224006 (2016).
- [38] P. Vogt and O. Bierwagen, *Appl. Phys. Lett.* **106**, 081910 (2015).
- [39] See Supplemental Material at <http://link.aps.org/supplemental/10.1103/PhysRevMaterials.6.033604> for additional information on experimental details, the effect of the In₂O₃ buffer layer, void formation at the film-substrate interface, and the method used to determine optical absorption onsets by raman spectroscopy.
- [40] G. Franceschi, M. Wagner, J. Hofinger, T. c. v. Krajňák, M. Schmid, U. Diebold, and M. Riva, *Phys. Rev. Mater.* **3**, 103403 (2019).
- [41] O. Bierwagen and J. S. Speck, *J. Appl. Phys.* **107**, 113519 (2010).
- [42] P. Vogt, Ph.D. thesis, Humboldt-Universität zu Berlin, 2017, doi: 10.18452/18036.
- [43] M. Birkholz, *Thin Film Analysis by X-ray Scattering* (Wiley-VCH, Weinheim, 2006).
- [44] K. H. L. Zhang, A. Regoutz, R. G. Palgrave, D. J. Payne, R. G. Egdell, A. Walsh, S. P. Collins, D. Wermeille, and R. A. Cowley, *Phys. Rev. B* **84**, 233301 (2011).
- [45] I. O. Mayboroda, A. A. Knizhnik, Y. V. Grishchenko, I. S. Ezubchenko, M. L. Zhanavskina, O. A. Kondratev, M. Y. Presniakov, B. V. Potapkin, and V. A. Ilyin, *J. Appl. Phys.* **122**, 105305 (2017).
- [46] Z. Galazka, R. Uecker, and R. Fornari, *J. Cryst. Growth* **388**, 61 (2014).
- [47] M. Feneberg, J. Nixdorf, C. Lidig, R. Goldhahn, Z. Galazka, O. Bierwagen, and J. S. Speck, *Phys. Rev. B* **93**, 045203 (2016).